Chapter VI

Ultrafast Transient Absorption Spectroscopy on Ni 2,2'-bipyridine Aryl Halide Complexes

Introduction

In recent decades, photoredox catalysis involving first-row transition metals has proliferated. Of particular interest is photoredox involving nickel catalysts, which has been demonstrated to provide access to C-C and C-heteroatom bond forming methodologies toward high-value synthetic products.[1–9] In some cases, these photoredox systems can perform couplings that are otherwise challenging for thermally driven Ni catalysis. Although some of these methodologies employ exogeneous photocatalysts such as Ir photosensitizers, recent reports have found that photoredox catalysis can be promoted using only Ni catalyst. As such, Ni complex excited states may play a significant role in the mechanisms of these photoredox cycles. This highlights the importance of understanding the relevant excited states and photodynamics of these Ni complexes.

Many of the relevant Ni catalysts that have been studied utilize 2,2'-bipyridine (bpy) and other bidentate diimine-type ligands. Recent work by the Doyle, Scholes, and Castellano groups have examined the transient absorption (TA) spectroscopy of various Ni(bpy)ArX complexes in which the bpy may be functionalized at the 4 and 4' positions.[10–12] The aryl group Ar may similarly be varied with substituents, but it is common to utilize kinetically stabilized variants that are functionalized in the *ortho*-position relative to the Ni-Ar bond. Finally, the X ligand can be varied between halides such as Cl and Br and O-atom ligating groups such as acetate (OAc). It was proposed that the initially excited ^{1}MLCT state quickly undergoes intersystem crossing within 5 – 10 ps followed by relaxation into a triplet ligand field [^{3}(d-d)] state. It was further proposed that Ni-C bond homolysis occurs from the transiently generated ^{3}(d-d) state as a part of the mechanistic cycle for these photocatalytic systems.

Recent reports have suggested from multireference *ab initio* calculations that the thermal barrier for bond homolysis is large (~70 kcal) from the [3](d-d) minimum energy point and proposed that higher lying repulsive potential energy surfaces may be involved in the bond homolysis.[13,14] A series of the Ni(bpy)ArX complexes were synthesized and studied with respect to their wavelength-dependent photodecomposition. We continue the characterization of some of these compounds here by fsTA to compare the relative rates of the photodynamic processes observed. We compare as well to the previous literature regarding the photophysics of these complexes and speak to some differences in the fittings we have obtained.

Results

Ni(tBu-bpy)(o-tolyl)Cl

We will begin with the discussion of the femtosecond transient absorption spectra of Ni(tBu-bpy)(*o*-tolyl)Cl (**1B**) and compare it to the previously reported spectra and fitted time constants. Selected time traces are shown in Figure 6.1.
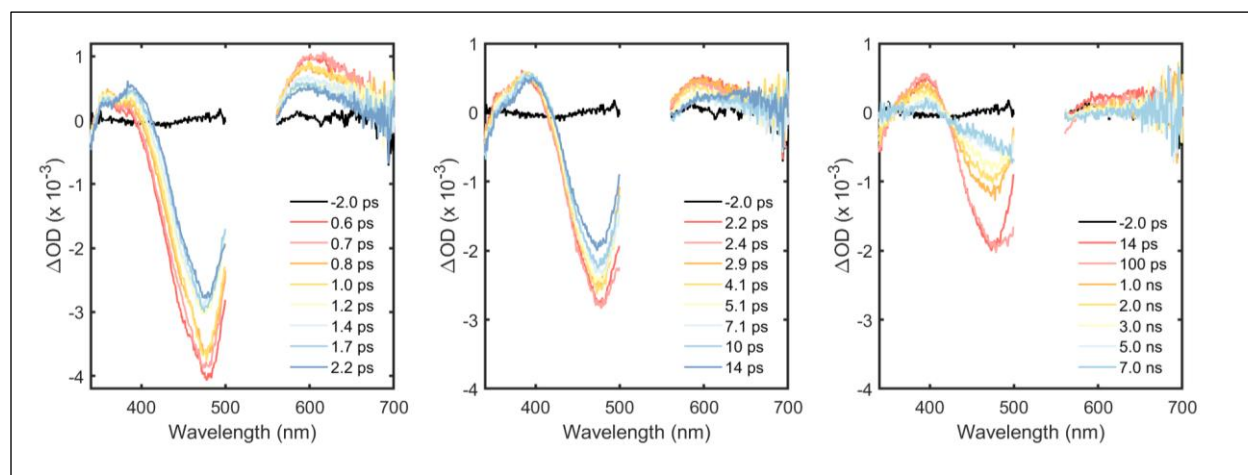
Figure 6.1 Transient absorption time traces of Ni(tBu-bpy)(*o*-tolyl)Cl across various time scales (left) 0.6 – 2.2 ps, (center) 2.2 – 14 ps, (right) 14 ps – 7 ns.

The initial transient features observed in the difference spectra of Ni(tBu-bpy)(*o*-tolyl)Cl after excitation with 530 nm light include a large bleach signal (GSB) centered around 480 nm near the maximum of the steady-state visible absorption spectrum flanked by excited state absorption (ESA) features in the 350 – 400 nm and 580 – 700 nm regions. Over the first 2.2 ps, the GSB feature decreases in intensity while the ESA features exhibit a time-dependent spectral shift. The 580 – 700 nm ESA decreases and blue shifts over the wavelength range, whereas the 350 – 400 nm ESA feature maximum around 360 nm decreases in intensity while the difference absorption (ΔA or ΔOD) increases at longer wavelengths around 380 nm, a red shift in ΔA maximum. In the time from 2.2 – 14 ps, the spectral shapes change little and we observe a monotonic decrease in the ΔA signals. By 14 ps, the 580 – 700 nm ESA signal has largely been reduced to zero. The transient spectrum continues to decay back to zero from 14 ps out to 7 ns.

The fsTA data matrix can be fit using global and target kinetic analysis. We fit the data using a four-component sequential model including a coherent artifact (CA) that persists around time zero. The evolution associated difference spectra (EADS) and weighted amplitudes of the fitted spectra are shown in Figure 6.2.
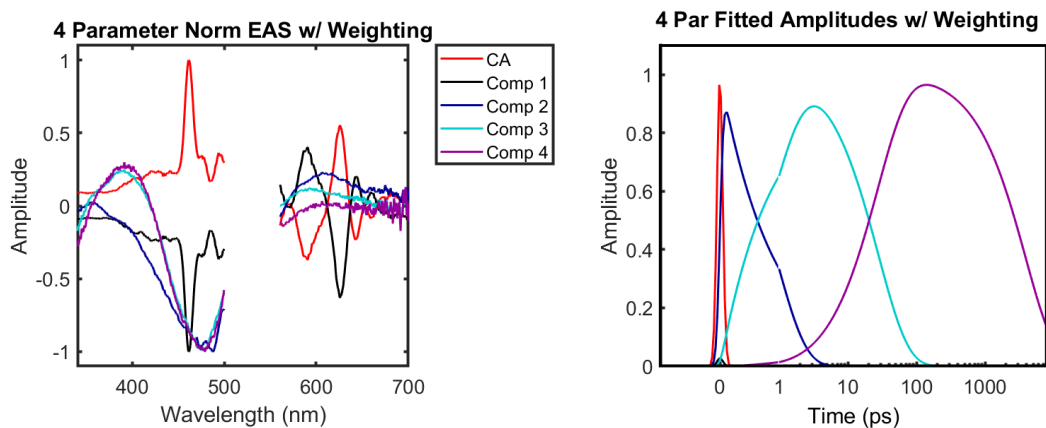
Figure 6.2 The EADS from fitting the Ni(tBu-bpy)(*o*-tolyl)Cl fsTA data matrix with a four-component sequential model (left) and the associated amplitude vectors (right).

As can be observed in the results of the fit, the first fitted component (Comp 1) has very little intensity and only persists around time zero. Additionally, the EADS of Comp 1 largely reflect the features in the fitted CA, which contains contributions from both oscillatory cross-phase modulation (XPM) as well as multiphoton coherent artifacts (large positive feature around 460 nm in CA, the position of this artifact is dependent on λ_{ex}). As such, this component does not realistically represent signal from the sample. However, attempts to fit with a three-component model generally led to bleed over of these coherent artifact features into the first component. The four-component model gave the best separation of these artifacts and the signal arising from the sample.

Components 2, 3, and 4 (Comp 2, Comp 3, Comp 4) reflect well the differences we observed across the various time scales of the data. For example, all three components share a negative feature around 480 nm consistent with the GSB observed in the time cuts. Comp 2 exhibits the ESA features on either side of the bleach, the higher energy ESA in Comp 2 has a

maximum near 360 nm, and the lower energy ESA a maximum near 620 nm. Comp 3, on the other hand, exhibits the higher energy ESA as having a maximum around 380 nm and the lower energy ESA having a maximum around 580 nm. This is consistent with the red and blue shifts observed in the higher energy and lower energy ESA features of the dataset over the first tens of picoseconds. Finally, Comp 4 is very similar to Comp 3 except with negligible ESA intensity in the 580 – 700 nm range, which is also consistent with what we observed in the 14 ps – 7 ns range. We plot the overlay of various time traces with the fits in Figure 6.3 as a means of assessing the quality of the fit. As observed, the fit is reasonably good across the time scales observed with some minor differences in intensity at early times.
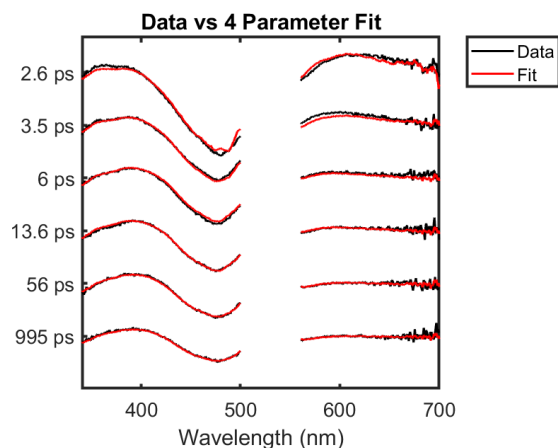

Figure 6.3 An overlay of the time cuts from the Ni(tBu-bpy)(*o*-tolyl)Cl fsTA dataset with time cuts of the fitted data matrix at 2.6, 3.5, 6, 13.6, 56, and 995 ps.

Finally, we compare the fitted rates and time constants with that reported by Doyle et al. In that report, the authors use a three-component sequential model to fit the data. As mentioned, the first component of our four-component model does not reflect signal arising from the sample,

so we compare time constants associated with Comps 2, 3, and 4 with the time constants of the previous report τ_1, τ_2, and τ_3. The results are listed in Table 6.1.

Table 6.1. Comparison of the rate and time constants obtained by fitting the Ni(tBu-bpy)(*o*-tolyl)Cl fsTA data with the previous report by Doyle et al.

	Our Experiment	Doyle et al. 2020		Our Experiment	Doyle et al. 2020
$k_1 (ps^{-1})$	1.1	1.5	$\tau_1 (ps)$	0.91	0.66
$k_2 (ps^{-1})$	0.036	0.145	$\tau_2 (ps)$	28.0	6.89
$k_3 (ps^{-1})$	0.000257	0.00025	$\tau_3 (ps)$	3900	4000

Our results compare favorably to the previous report. The first fitted time constant is around 1 ps in both cases (our experiment: 0.91 ps, Doyle et al. 2020: 0.66 ps). The second time constant displays the largest difference (our experiment: 28.0 ps, Doyle et al 2020: 6.89 ps). Finally, the third time constant is very similar (our experiment: 3900 ps, Doyle et al. 2020: 4000 ps). The second time constant seems to be closely associated with the loss of the low energy ESA feature in the spectrum. It is possible that better signal-to-noise in this region for our data (either by averaging or changing to a different probe beam) may improve the agreement between our data modeling and the reported values.

*Ni(COOCH$_3$-bpy)(*o*-tolyl)Cl*

The next compound we will discuss is Ni(COOCH$_3$-bpy)(*o*-tolyl)Cl. Here, the bipyridine is substituted by methyl ester in the 4 and 4' positions, which is more electron withdrawing relative to the *tert*-butyl substituents in the previous example. In the case of Ni(COOCH$_3$-bpy)(*o*-tolyl)Cl,

we chose to run successive experiments with increasing excitation energy as high energy excitation of the samples by LED lamps in prior photolysis studies exhibit greater product formation than low energy excitation. The steady-state absorption spectrum of Ni(COOCH$_3$-bpy)(o-tolyl)Cl along with a guide of the various excitation wavelengths is shown in Figure 6.4. In this trial, we ran the successive excitation wavelength experiments on the same sample, but further studies will probe the fsTA at each excitation wavelength on independent samples to remove any possible effects of prior photodegradation in the laser beam.
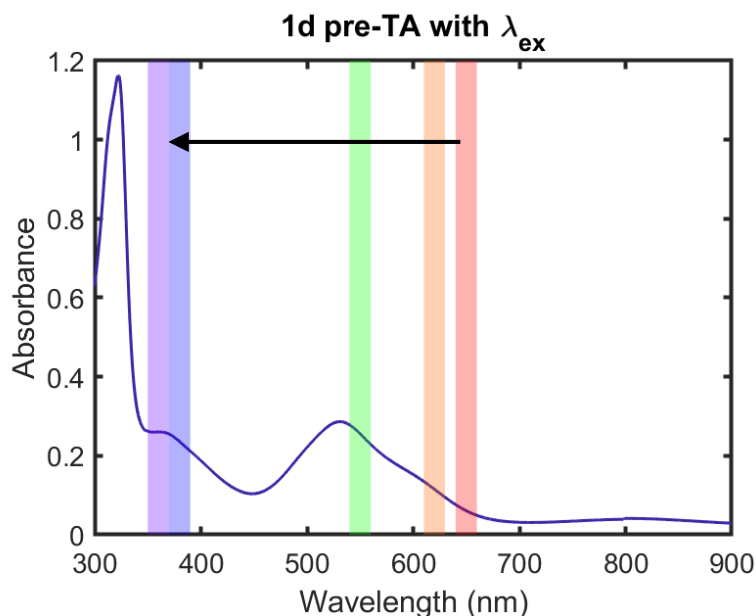

Figure 6.4 Steady-state absorption spectrum (pre-TA) of Ni(COOCH$_3$-bpy)(o-tolyl)Cl. The successive excitation wavelengths (λ_{ex}) examined are also denoted by color: 650, 620, 550, 380, 360 nm. Two runs were carried out at 650 nm, the first at 50 nJ/pulse and the second at 100 nJ/pulse. The rest of the experiments were carried out at 100 nJ/pulse save for the 380 nm experiment where the maximum power we were able to obtain at the sample was 80 nJ/pulse.

We will first show the fitting process and time cuts for the λ_{ex} = 650 nm dataset before comparing the results across the datasets collected. Initially we show the fsTA data at selected time cuts overlayed against a single component fit in Figure 6.5 along with the decay associated difference spectra (DADS) and associated fitted amplitudes.
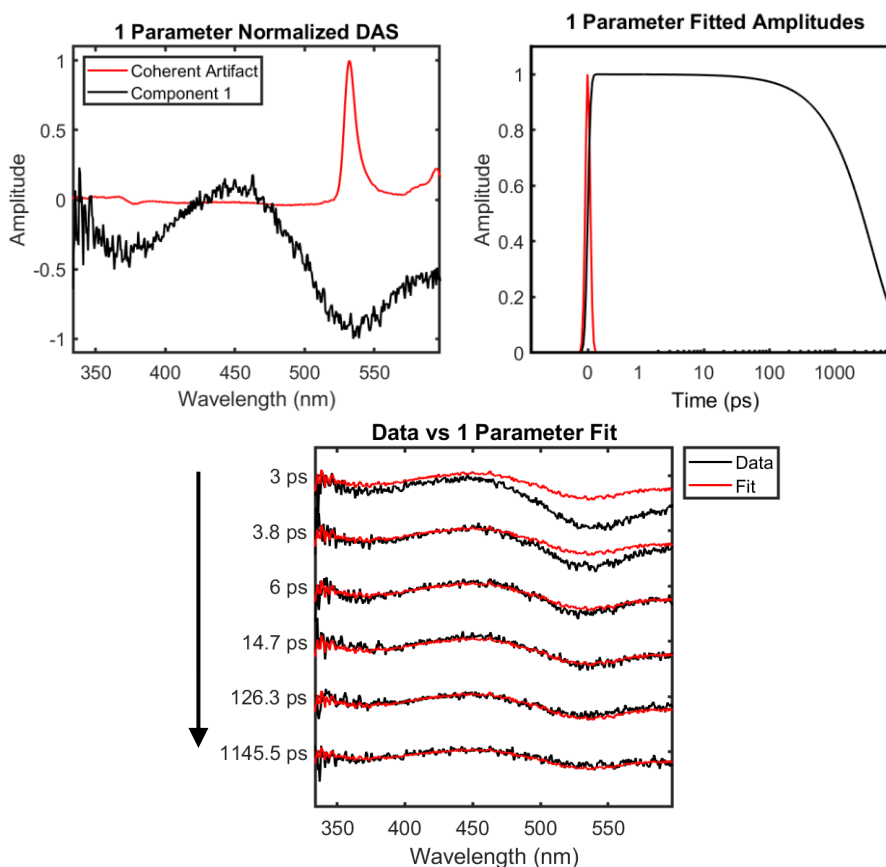

Figure 6.5 (Top left) The normalized DADS and (top right) associated amplitudes of the results from the one component global fitting of the data with a fitted coherent artifact. (Bottom) Overlay of the fsTA data with fitted data matrix time cuts at 3, 3.8, 6, 14.7, 126.3, and 1145.5 ps.

As seen in the time cuts of Figure 6.5, the major features of the fsTA spectra of Ni(COOCH$_3$-bpy)(o-tolyl)Cl include a negative GSB feature around 540 nm consistent with the

maximum of the MLCT transitions in the steady-state absorption spectrum. There is a slight positive feature around 450 nm observed as well and an additional bleach feature around 360 nm. The shape of the difference spectrum is consistent over the time scales observed. The single component global fit of the data yields a time constant for Component 1 of 3,750 ps. Although the DAS captures the spectrum at long times, as observed in the overlay, the single component model poorly fits the early time cuts of the dataset, particularly in the intensity of the GSB around 540 nm. This suggests that additional components are required to fit the data.

The results of a two-component sequential model fit are shown in Figure 6.6. Here, the data was weighted by a factor of 0.2 in the region from 2.3 to 2.7 ps and 520 to 585 nm, which covers the time and wavelength region of the sharp coherent artifact centered around 530 nm. Without this weighting factor, the first component DADS contained contribution from this coherent feature.
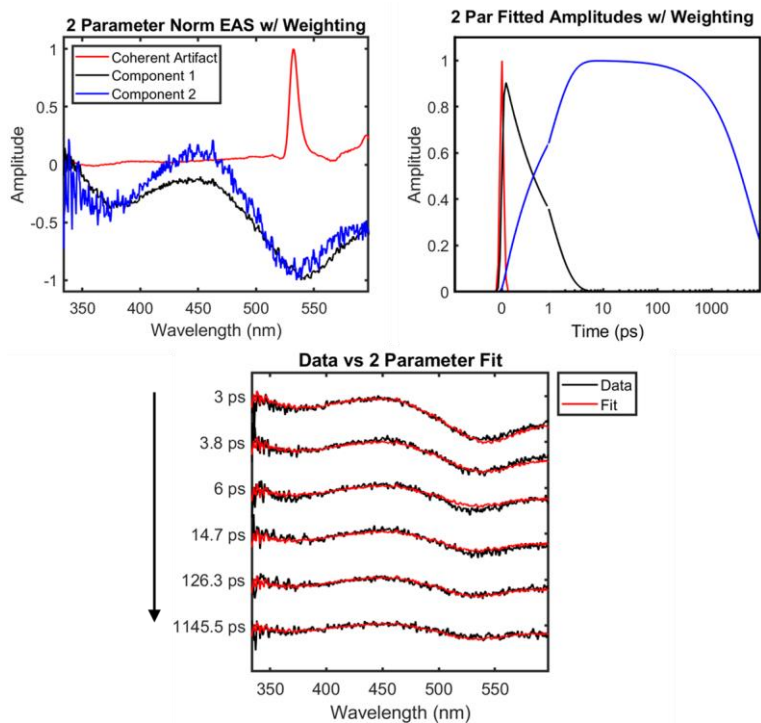
Figure 6.6 (Top left) The normalized EADS and (top right) associated amplitudes of the results from the fit of the data to a two-component sequential model with a fitted coherent artifact. (Bottom) Overlay of the fsTA data with fitted data matrix time cuts at 3, 3.8, 6, 14.7, 126.3, and 1145.5 ps.

As observed in the overlays, the two-component model provides a better fit of the data across all time scales. The time constants associated with components 1 and 2 are 0.972 and 5,130 ps, respectively. We repeated this fitting process for all of the datasets taken on the $Ni(COOCH_3\text{-}bpy)(o\text{-}tolyl)Cl$ sample. We summarize and compare the results in Table 6.2 and Figure 6.7.

Table 6.2. Comparison of the two-component sequential model fits of the various λ_{ex} experiments on Ni(COOCH$_3$-bpy)(*o*-tolyl)Cl.

|	k_1 (ps^{-1})	k_1 error	k_2 (ps^{-1})	k_2 error	τ_1 (ps)	τ_2 (ps)
650 nm, 50 μW	0.75232	0.01434	0.000148093	0.000002584	1.32922	6752.51
650 nm, 100 μW	0.817024	0.009809	0.000219954	0.00000251	1.22395	4546.41
620 nm, 100 μW	1.02869	0.00621	0.000195029	0.000001227	0.972107	5127.44
550 nm, 100 μW	1.29303	0.00625	0.000187795	0.000001051	0.773375	5324.96
380 nm, 80 μW	1.01451	0.006165	0.000196895	8.041E-07	0.9857	5078.85
360 nm, 100 μW	0.311567	0.001667	0.000152447	7.499E-07	3.20959	6559.68
Average	0.869524		0.000183369		1.415657	5564.975
Std. Dev.	0.332722		2.78479E-05		0.900727	885.7216
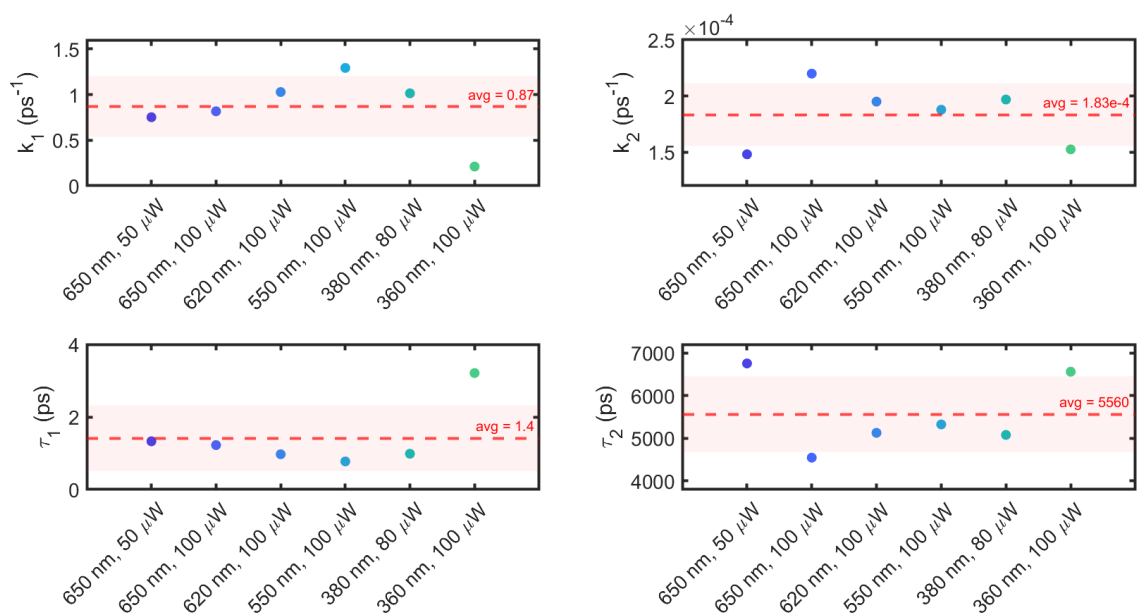
Figure 6.7 Comparison of the rate and time constants detailed in Table 7.2. The average and single standard deviation are denoted by the dashed red line and shaded red area respectively.
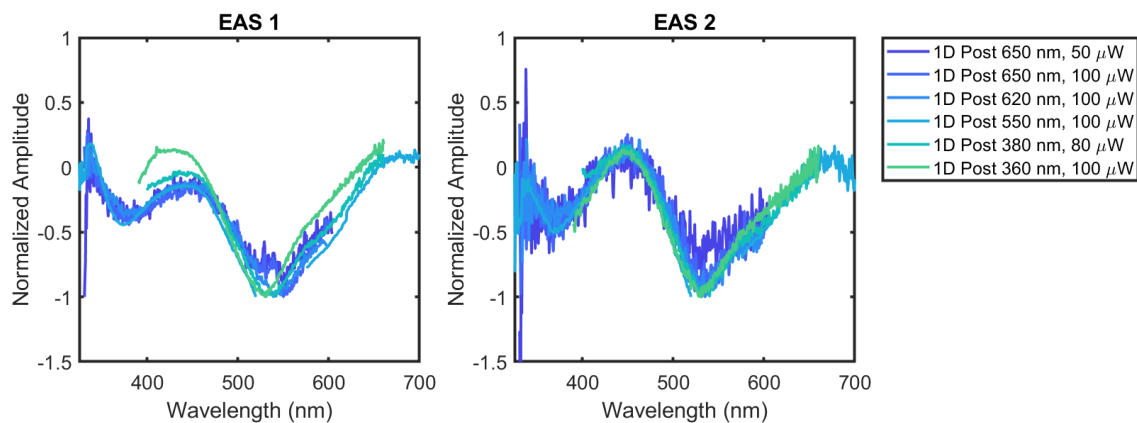

Figure 6.8 Overlay of the EADS 1 and 2 for each of the λ_{ex} experiments carried out on Ni(COOCH$_3$-bpy)(o-tolyl)Cl.

As can be seen in Table 6.2, Figure 6.7 and Figure 6.8, the fitted rate constants are consistent across the collected datasets. The main outlier is that collected at 360 nm. Nevertheless, the EADS are all consistent with each other. Attempts to fit the datasets to three-component models were unsuccessful. This contrasts with the Ni(tBu-bpy)(o-tolyl)Cl fsTA data, which required a three-component model. Assuming that the excited state relaxation processes are the same between the two Ni-bipyridine complexes, it is possible that the fastest relaxation process is too fast to observe in Ni(COOCH$_3$-bpy)(o-tolyl)Cl given the time resolution of our instrument (~100 fs).

Power titrations were collected at λ_{ex} = 550 and 380 nm. At 550 nm, the powers investigated were 50, 100, 250, 500, and 800 µW (or nJ/pulse). The ΔA values collected at four wavelength positions across the spectrum around 2 ps time delay are plotted versus applied power in Figure 7.X. The trend in ΔA values with power confirms that our studies fall within the linear regime.
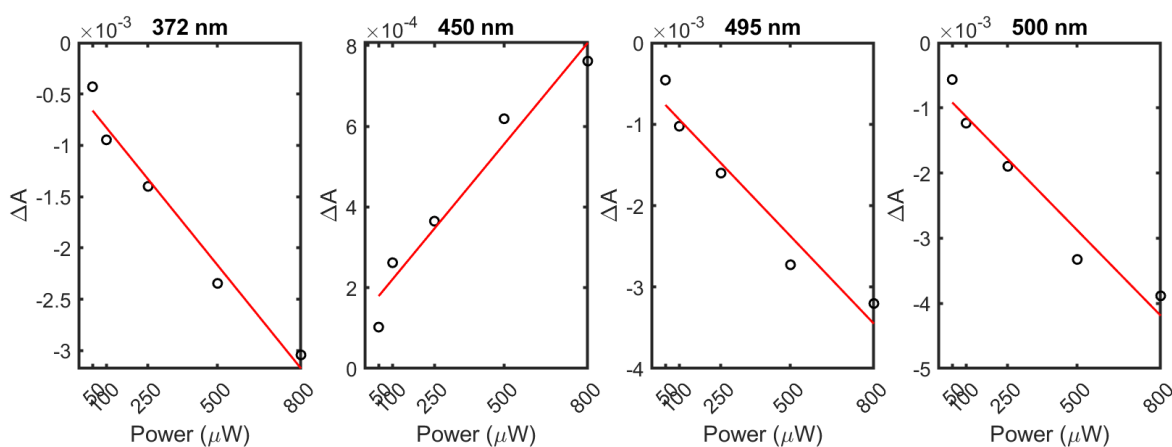

Figure 6.9 Power dependence of the Ni(COOCH$_3$-bpy)(o-tolyl)Cl ΔA signal at 372, 450, 495, and 500 nm. The red line represents the linear fit of the data points.

To examine the time traces and general kinetics at each power, we overlay the normalized time traces observed at 450 nm in Figure 7.X and show that the kinetics do not diverge significantly with changing power.
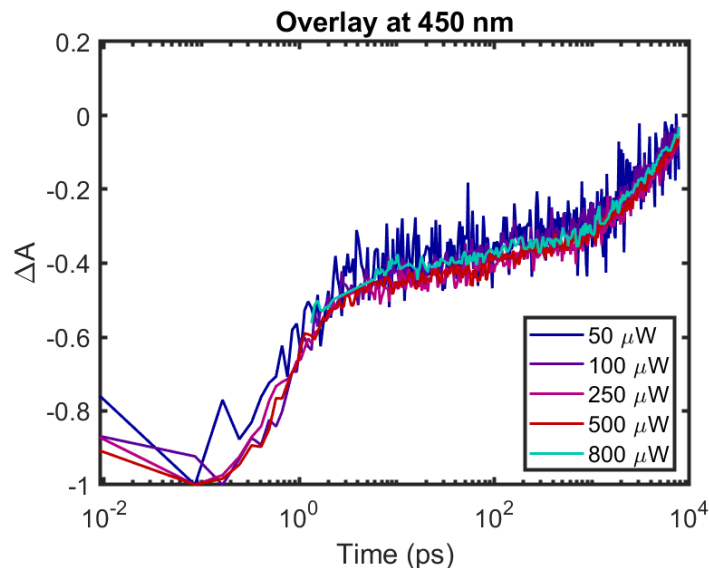

Figure 6.10 Overlay of the time traces observed at 450 nm collected for the Ni(COOCH$_3$-bpy)(o-tolyl)Cl fsTA data at each power.

Ni(tBu-bpy)(mesityl)Br

We also examined the more sterically encumbered complex Ni(tBu-bpy)(mesityl)Br. The fitting results and time cuts for a 3 parameter sequential model are shown in Figure 6.11. As with Ni(tBu-bpy)(o-tolyl)Cl, the first time component only has small amplitude within the instrument response and contains mostly features associated with coherent artifacts around time zero. The inclusion of this additional component helped to separate these coherent artifact features from the other fitted components.
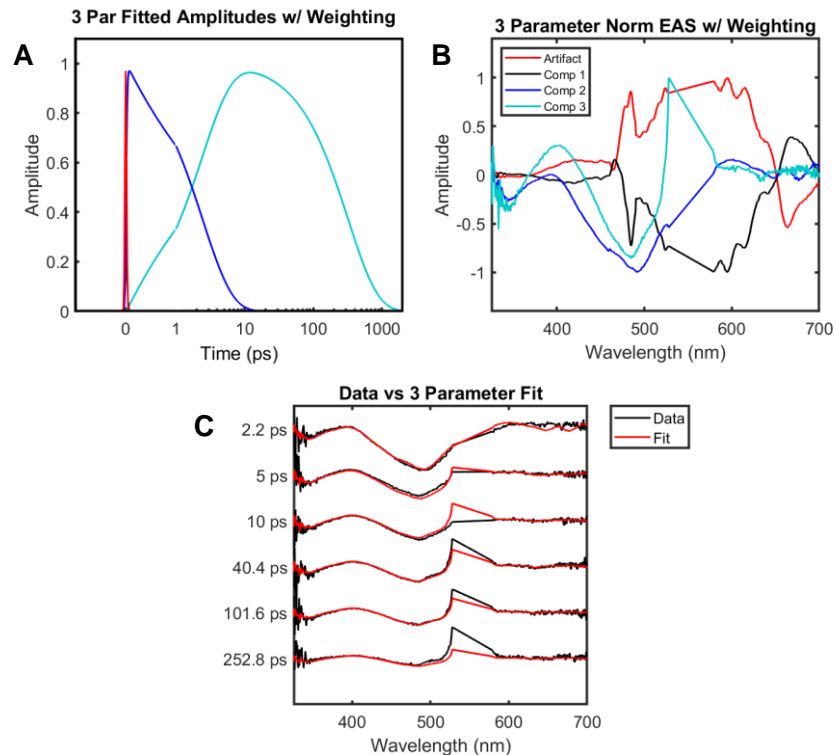
Figure 6.11 The results of a three-component sequential model fit to the Ni(*t*Bu-bpy)(mesityl)Br fsTA dataset. (**A**) The amplitudes of the fitted components along with a fitted coherent artifact (in red) (**B**) The normalized EADS of the fitted components along with a fitted coherent artifact (**C**) An overlay of the three-component model fit (in red) over spectral traces of the data (in black).

The results of the three-component fitting yield time constants $\tau_1 = 10.5$ fs, $\tau_2 = 2.44$ ps, and $\tau_3 = 323$ ps. As mentioned, we take the first time component to be unrelated to the dynamics of the complex. The other two time components are reasonable given the dataset. We note that the low energy region of the spectrum is still not fit well at the earliest times (see 2.2 ps in Figure 6.11C). As previously discussed with respect to this region, further averaging or a different probe could improve the signal-to-noise in this region, which could help better fit it. This could be a result of oscillatory features in the cross phase modulation bleeding over into Comp 2 of the fit.

164

The first time component (2.44 ps) is consistent with the fast decay component observed in the fsTA datasets of the previous Ni complexes. The second time component (323 ps) is, however, significantly faster than those observed in the other complexes (typically the signal persists out to several nanoseconds). In the case of Ni(tBu-bpy)(mesityl)Br, the transient signal is fully decayed by 2 ns.

Discussion and Summary

We have reported here the fsTA data for three Ni(bpy)ArX complexes: Ni(tBu-bpy)(o-tolyl)Cl, Ni(COOCH$_3$-bpy)(o-tolyl)Cl, and Ni(tBu-bpy)(mesityl)Br. The general features observed in the difference spectra are similar with a prominent ground state bleach signal in the 450 – 550 nm region flanked by weaker excited state absorptions on the low and high energy sides. The datasets were fitted with target kinetic analyses, yielding rate constants comparable to those reported for related complexes. In general, there is a faster time component on the order of ~1 ps, a middle time component on the order of 5 – 10 ps, which have been difficult to accurately fit, and a longer lived time component that spans out to several nanoseconds.

Ni(tBu-bpy)(mesityl)Br stands in contrast as the excited state population decays much more quickly back to the ground state and is fully returned by 2 ns. This could potentially arise from the mesityl group that may restrict conformational changes in the molecule. For example, we expect that relaxation into a metal-centered ^{3}(d-d) state would encourage a square planar to tetrahedral distortion in the ligand coordination geometry. The mesityl group may prohibit the rotation required to achieve this. Potential agostic interactions between the Ni and methyl C-H bonds may also stabilize the ^{3}(d-d) relative to the singlet ground state, promoting faster nonradiative decay.

Citations

(1)   Twilton, J.; Le, C. (Chip); Zhang, P.; Shaw, M. H.; Evans, R. W.; MacMillan, D. W. C. The Merger of Transition Metal and Photocatalysis. *Nat Rev Chem* **2017**, *1* (7), 1–19. https://doi.org/10.1038/s41570-017-0052.

(2)   Milligan, J. A.; Phelan, J. P.; Badir, S. O.; Molander, G. A. Alkyl Carbon–Carbon Bond Formation by Nickel/Photoredox Cross-Coupling. *Angewandte Chemie International Edition* **2019**, *58* (19), 6152–6163. https://doi.org/10.1002/anie.201809431.

(3)   Narayanam, J. M. R.; Stephenson, C. R. J. Visible Light Photoredox Catalysis: Applications in Organic Synthesis. *Chem. Soc. Rev.* **2010**, *40* (1), 102–113. https://doi.org/10.1039/B913880N.

(4)   Prier, C. K.; Rankic, D. A.; MacMillan, D. W. C. Visible Light Photoredox Catalysis with Transition Metal Complexes: Applications in Organic Synthesis. *Chem. Rev.* **2013**, *113* (7), 5322–5363. https://doi.org/10.1021/cr300503r.

(5)   Koike, T.; Akita, M. Visible-Light Radical Reaction Designed by Ru- and Ir-Based Photoredox Catalysis. *Inorg. Chem. Front.* **2014**, *1* (8), 562–576. https://doi.org/10.1039/C4QI00053F.

(6)   Shaw, M. H.; Twilton, J.; MacMillan, D. W. C. Photoredox Catalysis in Organic Chemistry. *J. Org. Chem.* **2016**, *81* (16), 6898–6926. https://doi.org/10.1021/acs.joc.6b01449.

(7)   Heitz, D. R.; Tellis, J. C.; Molander, G. A. Photochemical Nickel-Catalyzed C–H Arylation: Synthetic Scope and Mechanistic Investigations. *J. Am. Chem. Soc.* **2016**, *138* (39), 12715–12718. https://doi.org/10.1021/jacs.6b04789.

(8)   Welin, E. R.; Le, C.; Arias-Rotondo, D. M.; McCusker, J. K.; MacMillan, D. W. C. Photosensitized, Energy Transfer-Mediated Organometallic Catalysis through Electronically Excited Nickel(II). *Science* **2017**, *355* (6323), 380–385. https://doi.org/10.1126/science.aal2490.

(9)   Kudisch, M.; Lim, C.-H.; Thordarson, P.; Miyake, G. M. Energy Transfer to Ni-Amine Complexes in Dual Catalytic, Light-Driven C–N Cross-Coupling Reactions. *J. Am. Chem. Soc.* **2019**, *141* (49), 19479–19486. https://doi.org/10.1021/jacs.9b11049.

(10)   Shields, B. J.; Kudisch, B.; Scholes, G. D.; Doyle, A. G. Long-Lived Charge-Transfer States of Nickel(II) Aryl Halide Complexes Facilitate Bimolecular Photoinduced Electron Transfer. *J. Am. Chem. Soc.* **2018**, *140* (8), 3035–3039. https://doi.org/10.1021/jacs.7b13281.

(11)   Ting, S. I.; Garakyaraghi, S.; Taliaferro, C. M.; Shields, B. J.; Scholes, G. D.; Castellano, F. N.; Doyle, A. G. 3d-d Excited States of Ni(II) Complexes Relevant to Photoredox Catalysis: Spectroscopic Identification and Mechanistic Implications. *J. Am. Chem. Soc.* **2020**, *142* (12), 5800–5810. https://doi.org/10.1021/jacs.0c00781.

(12)   Yang, L.; Lu, H.-H.; Lai, C.-H.; Li, G.; Zhang, W.; Cao, R.; Liu, F.; Wang, C.; Xiao, J.; Xue, D. Light-Promoted Nickel Catalysis: Etherification of Aryl Electrophiles with Alcohols Catalyzed by a NiII-Aryl Complex. *Angewandte Chemie International Edition* **2020**, *59* (31), 12714–12719. https://doi.org/10.1002/anie.202003359.

(13)   Cagan, D. A.; Stroscio, G. D.; Cusumano, A. Q.; Hadt, R. G. Multireference Description of Nickel–Aryl Homolytic Bond Dissociation Processes in Photoredox Catalysis. *J. Phys. Chem. A* **2020**, *124* (48), 9915–9922. https://doi.org/10.1021/acs.jpca.0c08646.

(14)   Cagan, D. A.; Bím, D.; Silva, B.; Kazmierczak, N. P.; McNicholas, B. J.; Hadt, R. G. Elucidating the Mechanism of Excited-State Bond Homolysis in Nickel–Bipyridine Photoredox Catalysts. *J. Am. Chem. Soc.* **2022**. https://doi.org/10.1021/jacs.2c01356.